Spray Combustion Simulation Study of Waste Cooking Oil Biodiesel and Diesel under Direct Injection Diesel Engine Conditions.

*Olawole Abiola Kuti[a]
o.kuti@mmu.ac.uk

S. Mani Sarathy[b]
mani.sarathy@kaust.edu.sa

K. Nishida[c]
nishida@hiroshima-u.ac.jp

[a]Department of Engineering, Faculty of Science and Engineering, The Manchester Metropolitan University, John Dalton Building, Chester Street, Manchester M1 5GD, United Kingdom

[b]King Abdullah University of Science and Technology (KAUST), Clean Combustion Research Center (CCRC), Thuwal 23955-6900, Saudi Arabia

[c]Department of Mechanical System Engineering, University of Hiroshima, Higashi-Hiroshima 739-8527, Japan

*Corresponding Author
Tel. No.: +447491648546
[a]Department of Engineering, Faculty of Science and Engineering, The Manchester Metropolitan University, John Dalton Building, Chester Street, Manchester M1 5GD, United Kingdom

Spray Combustion Simulation Study of Waste Cooking Oil Biodiesel and Diesel under Direct Injection Diesel Engine Conditions.

Abstract

Spray and combustion characteristics of waste cooking oil biodiesel (WCO) and conventional diesel fuels were simulated using a RANS (Reynolds Averaged Navier Stokes) based model. Surrogates were used to represent WCO and diesel fuels in simulations. *N*-tetradecane ($C_{14}H_{30}$) and *n*-heptane (C_7H_{16}) were used as surrogates for diesel. Furthermore, for WCO, surrogate mixtures of methyl decanoate, methyl-9-decenoate and *n*-heptane were used. Thermochemical and reaction kinetic data (115 species and 460 reactions) were implemented in the CFD code to simulate the spray and combustion processes of the two fuels. Validation of the spray liquid length, ignition delay, flame lift-off length and soot formation data were performed against previous published experimental results. The modeled data agreed with the trends obtained in the experimental data at all injection pressures. Further investigations, which were not achieved in previous experiments, showed that prior to main ignition, a first stage ignition (cool flame) characterized by the formation formaldehyde (CH_2O) species at low temperature heat release occurred. The main ignition process occurred at high temperature with the formation of OH radicals. Furthermore, it was observed that the cool flame played a greater role in stabilizing the downstream lifted flame of both fuels. Increase in injection pressure led to the cool flame location to be pushed further downstream. This led to flame stabilization further away from the injector nozzle. WCO had shorter lift-off length compared to diesel as a result of its cool flame which being closer to the injector. Soot formation followed similar trends obtained in the experiments.

Keyword: Simulation; Spray; Combustion; Waste Cooking Oil Biodiesel (WCO); Diesel; Diesel Engine Conditions

1. Introduction

Diesel engine plays a vital role in transportation due to its high efficiency. However, emissions from diesel engine are detrimental to health and environment. In ensuring a cleaner and safer environment, organizations such as the US EPA and EU are proposing stringent limits on original engine manufacturers (OEM). For example, the European Union has proposed the Euro 6d-temp emission limits for both passenger cars and heavy duty vehicles [1]. It is expected that these regulations will become more stringent with time.

Current heavy-duty diesel engine operates between injection pressures of 2000 to 2500 bars. Experimental works have revealed that by increasing injection pressure to ultra-high value of 3000 bars, noxious emissions produced by diesel engine could be minimized [2,3]. Therefore, higher injection pressures and biofuels such as biodiesel could be effective in reducing emissions in diesel engine in realizing the targets set by environmental bodies [4,5]. In context of reducing particulate matter and other emissions, there are prospects of using biodiesel as an alternative fuel in diesel. However, there have been major concerns on biodiesel production since its feedstock is in competition with food supply [6]. A solution to this problem is by recycling used cooking oil from food industries and restaurants. The recycled used cooking oil, which are not expected to be in competition with food supplies, can be used as feedstock to produced waste cooking oil biodiesel (WCO) through esterification processes. Due to its high oxygen content, WCO has prospects of being a better candidate for reducing emissions in diesel engine. Experimental works have revealed that by increasing injection pressure up to ultra-high value of 300 MPa, particulate emissions can be reduced in diesel engine [7-10]. Furthermore, palm biodiesel spray and combustion characteristics such as liquid length, gas entrainment, flame structures and soot formation under the influence of ultra-high injection of 300 MPa have been investigated in previous works by the authors [4, 5]. Intermediate species are usually produced since combustion in

diesel engine involves chemical processes. Intermediate products such as formaldehyde (CH_2O) and hydroxyl radical (OH*) species are of high importance since they are precursors of low and high release processes respectively in advanced combustion systems. Several works to mention a few, have reported on the prospects of using WCO in diesel engine. As an alternative to diesel, WCO has been found to produce lower level of harmful emissions with similar engine performance [11-12]. As reported by [13], smoke emissions sharply decreased with increase in biodiesel concentration with no significant change in engine efficiency when two different cases of WCO-diesel blends were investigated. It was concluded that WCO was better in reducing HC, CO and smoke emissions as injection pressure increased however while NO_x emission increased at all experimental conditions. The performance, emission and combustion characteristics of a single cylinder diesel engine fuelled with WCO-diesel blends at various volumetric concentration were investigated in the work reported by [14]. As compression ratio increased, it was observed that WCO-diesel blends tends to have longer ignition delay, maximum rate of pressure rise, lower heat release rate and higher mass fraction compared to conventional diesel fuel. All these studies have focused on engine testing with no optical accessibility, which is not suitable for investigating flame structures and spray flame interactions. Furthermore, these studies did not provide sufficient information on the underlying fundamental phenomena such as mixture formation and chemical kinetics, which could influence spray combustion processes of WCO. The use of optical diesel engine test rig to investigate the spray, combustion and emission characteristics of neat WCO and diesel have been reported by [15-16]. It was observed in these works that WCO exhibited longer liquid penetration length and narrower spray angle than diesel. Due to poor atomization, WCO displayed longer ignition delay with a slightly lower peak of in-cylinder pressure and heat release rate than diesel with reduction in carbon monoxide, unburned hydrocarbon and particulate matter emissions. While optical engines

were used in the works mentioned earlier, flame structures with spray flame interactions of WCO were not addressed. In addition, due to cycle-to-cycle variations in engine test cells, which could lead to variations in ambient conditions, the feasibilities of investigating flame structures of fuels are limited. Hence, fundamental studies using specialized rig such as the constant volume vessel, which can mimic real engine conditions without creating cycle-to-cycle variations, become inevitable. Spray flame interactions in fuels for diesel engines are important in understanding the physical and chemical processes occurring upstream of a lifted flames and their subsequent effects on soot formation occurring downstream. However, there is no significant study on fundamental studies, which can provide adequate information on flame structures and spray flame interactions in WCO. Fundamental study using the constant volume vessel by [17] focused on ignition, flame lift-off length and emission of diesel fuel blended with hydrogenated catalytic biodiesel from WCO. While the flame structures of the blends and pure WCO in terms of OH* chemiluminescence were reported in [17], spray flame interactions were not investigated. Furthermore, fuel injection pressures in these studies are low compared to what is being proposed for future production engines, which is expected to be above 200 MPa. With all these shortcomings, it becomes imperative to investigate further the role of intermediate species on heat release and the stabilization of WCO flames under diesel engine conditions as injection pressure increases to 300 MPa. Also because of spray flame interactions that are inevitable in diesel engine, there is the need to investigate further the impact of mixture formation on auto-ignition and subsequent combustion events as injection pressure increased to 300 MPa. Therefore, in this research, the use of computational fluid dynamics with chemical kinetics tool has prospects for investigating further intermediate species formation and spray-flame interactions of WCO under diesel engine conditions. It is envisaged that the role of fuel properties such as viscosity, cetane number and molecular oxygen content on formation of intermediate products and

spray-flame interactions of WCO compared to conventional diesel fuel will be investigated. Results from this research are expected to be of benefits to fuel scientists in understanding spray and combustion characteristics of WCO in diesel engine taking into consideration its physical and chemical properties as compared to conventional diesel fuel. Furthermore, in realising the future emission reduction goals set by various countries, there are tendencies that fuel injection pressure in current heavy-duty engines will be increased to ultra-high value of 300 MPa. Therefore, this research will be of benefits to original equipment manufacturers (OEMs) in designing diesel engine that could utilize alternative fuel such as WCO whose properties are different from conventional diesel engine.

2. Computational Model Set-up and Validation

In this study, spray combustion simulations were performed by employing the Eulerian-Lagrangian approach using a proprietary computational fluid dynamics (CFD) code fully described in [18]. This code has the capability of incorporating spray injection, atomization and breakup, turbulence, droplets collision models with a chemical kinetic solver. The gas-phase flow field is described using the Favre-averaged Navier-Stokes (a variant of the Reynolds Navier Stokes (RANS)) with the renormalization group theory (RNG) k-ε turbulence model. The RNG k- ε turbulence model includes the source terms for the effects of the dispersed phase on gas phase turbulence. A brief description of the RANS turbulence model is provided in this study. Further details can be obtained in [18] and from previous works reported in [19-20]. The RANS Favre-averaged compressible mass transport is given as;

$$\frac{d\bar{\rho}}{dt} + \frac{\partial \bar{\rho}\tilde{u}_j}{\partial x_j} = 0 \tag{1}$$

while the momentum transport is given as;

$$\frac{d\bar{\rho}\tilde{u}_i}{dt} + \frac{\partial \bar{\rho}\tilde{u}_i\tilde{u}_j}{\partial x_j} = \frac{\partial \bar{P}}{\partial x_i} + \frac{\partial}{\partial x_j}\left[\mu\left(\frac{\partial \tilde{u}_i}{\partial x_j} + \frac{\partial \tilde{u}_j}{\partial x_i}\right) - \frac{2}{3}\mu\frac{\partial \tilde{u}_k}{\partial x_k}\delta_{ij}\right] + \frac{\partial}{\partial x_j}\left(-\bar{\rho}\widetilde{u_i'' u_j''}\right) \tag{2}$$

where the Favre average is defined for velocity as;

$$\tilde{u}_j \equiv \frac{\overline{\rho u_\iota}}{\bar{\rho}} \tag{3}$$

The ensemble averaging of the equations introduces additional terms called the Reynold stresses that represent the effect of turbulence. The Reynold stress τ_{ij} i.e. the sub-grid stress tensor included in the last term in equation (2) is given by;

$$\tau_{ij} = -\bar{\rho}\widetilde{u_\iota^{'} u_j^{'}} \tag{4}$$

The turbulence model must model the Reynolds stress to obtain the closure for equation (2). The modelled Reynold stress for the RNG k- ε model is given by;

$$\tau_{ij} = -\bar{\rho}\widetilde{u_\iota^{'} u_j^{'}} = 2\mu_t S_{ij} - \frac{2}{3}\delta_{ij}\left(\rho k + \mu_t \frac{\partial \tilde{u}_j}{\partial x_i}\right) \tag{5}$$

The turbulent kinetic energy k, is defined as half of the trace of the stress tensor:

$$k = \frac{1}{2}\widetilde{u_\iota^{'} u_j^{'}} \tag{6}$$

where the turbulent viscosity, μ_t, is given by ;

$$\mu_t = C_\mu \rho \frac{k^2}{\varepsilon} \tag{7}$$

C_μ is a model constant for the fluid flow and ε is the dissipation of turbulent kinetic energy. Also the mean the strain rate tensor S_{ij} is given by;

$$S_{ij} = \frac{1}{2}\left(\frac{\partial \tilde{u}_i}{\partial x_j} + \frac{\partial \tilde{u}_j}{\partial x_i}\right) \tag{8}$$

In addition to all these equation, spray formation was simulated by employing the blob injection method of Reitz and Diwakar [21] in which parcels of liquid with a characteristic size equal to the effective nozzle diameter are injected into the computational domain. Primary atomization of the liquid blobs and subsequent droplets (secondary atomization) are simulated with models based on the Kelvin-Helmholtz (KH) and Rayleigh-Taylor (RT) instability mechanisms [22]. Droplet collision was based on no time counter (NTC) algorithm

of Schimdt and Rutland [23] while collisions were predicted as bouncing, stretching, reflexively separating or coalescing [24]. A droplet evaporation model based on the Frossling correlation was used to convert the injected liquid spray in the computational domain into gaseous vapor. The Taylor Analogy Breakup (TAB) model was implemented in the spray model to determine the droplet drag coefficient. This accounts for the drop distortion that could vary linearly between the drag on a sphere and a disk. Full details and definition of spray models have been described extensively in [18]. In treating the combustion aspect of the simulation, the SAGE detailed chemical kinetics solver, which models chemical kinetics via sets of CHEMKIN-formatted input files were utilized. The SAGE detailed chemical kinetic solver is coupled directly with the gas-phase calculations using a well-stirred reactor model. To accelerate numerical solution, the multi-zone model solves the SAGE detailed chemical kinetics in zones i.e. group of cells that have similar thermodynamic state. With all the models, these equations earlier defined were solved numerically using a finite volume solver. Normal tetradecane (*n*-$C_{14}H_{30}$) and normal heptane (*n*-C_7H_{16}) were selected as surrogates for diesel to capture the fuel physical and chemical properties respectively. For the WCO surrogate composition, methyl decanoate, methyl-9- decenoate and *n*-heptane were combined in proportions based on previous GC-MS results reported in [25] for the five major biodiesel components. The five major biodiesel components are methyl palmitate ($C_{17}H_{34}O_2$), methyl stearate ($C_{19}H_{38}O_2$), methyl oleate ($C_{19}H_{36}O_2$), methyl linoleate ($C_{19}H_{34}O_2$) and methyl linolenate ($C_{19}H_{32}O_2$). The choice of methyl decanoate ($C_{11}H_{22}O_2$; surrogate with single bond in its hydrocarbon chains), methyl-9-decenoate ($C_{11}H_{20}O_2$; surrogate with double bond in its hydrocarbon chains) and *n*-heptane for WCO surrogate has been reported in previous work [26] on a robust detailed reaction mechanism (3034 species and 8580 reactions) for biodiesel fuels . Table 1 presents the composition and formulation of the WCO surrogate based on the five major biodiesel components. In Table 1, each biodiesel major

component is formulated by combining the surrogates in proportion that is approximate to the number of its molecules. In achieving the formulation, the type of hydrocarbon chain whether saturated (single bond) or unsaturated (double bond) is taken into consideration. Zhaoyu and co-workers [27] further reduced the detailed reaction mechanism by [26] to 115 species and 460 reactions for diesel and biodiesel spray combustion simulations. The OH* (hydroxyl radical) mechanism by Kathriota [28] was added to the diesel and biodiesel mechanisms in order to capture the ignition and lifted flame structures. Soot simulation within the computation cell were determined from a single-step competition between the formation and oxidation rates of C_2H_2 species based on the empirical Hiroyasu model coupled with the Nagle and Strickland-Constable models [29-30]. A cylindrical geometry of 60 mm in diameter and 120mm in length was used for the simulation to describe the section of the constant volume chamber used in the experiment. Figure 1 shows the CAD profile of the section of the constant volume chamber used for the simulation. The grid (adaptive mesh refinement and base grid cells) which are generated internally during the run time is also presented alongside. The base grid was fixed at 2 mm. Levels of adaptive mesh refinement are employed for the velocity field such that a minimum grid size is achieved. This is desirable in achieving refined grids through the addition of grid resolution locally in critical flow regions of the domain while leaving other sections relatively coarse (i.e. base grids). In resolving complex flow behavior around the nozzle through adaptive mesh refinement, an extra resolution using a nozzle and injector fixed grid embedding was utilized. As shown in Fig. 1, the extra resolutions made the grid points at the nozzle boundary finer while other locations that are not important were left coarse. The relationship for the minimum cell size, dx required for adaptive refinement with the base grid size, dx_{base} and the embedded scale has been defined in [31] as;

$$dx = dx_{base} * 2^{-(embed\ scale)} \quad (9)$$

Summary of the parameters used for the numerical studies are presented in Table 2. Simulation was performed using computing nodes on the Cray XC Shaheen-II high performance computing (HPC) facility. The HPC has a speed of 7.2 petaflop at theoretical peak performance and 6174 nodes with each node having a memory of 128 GB.

Simulation input parameters such as ambient gas, nozzle diameter and injection pressure are based on conditions described in previous experiments [4, 5]. In order to capture the events that took place after the end of injection, simulation time for combustion was extended to 2.2ms. Based on previous experiments, fuel injection duration was maintained at 1.5 ms ASOI (after start of injection). Simulated results were validated against experimental results obtained in previous experiments [5]. Details of the parameters taken into consideration during simulation activities are presented in Table 2. Furthermore, Table 3 presents the properties of the fuel used in the experiment as reported in [4, 5].

3. Results and Discussion

3.1 Grid Convergence Study

Extensive studies on grid convergence have been reported in previous works by [31]. The minimum cell size suitable for simulation as stated in [31] has been reported in previous study by the authors in [32]. However, in this study, an evaporating spray case is presented to assess the minimum cell suitable for the convergence behaviour of the liquid length. It should be noted that the chemistry solver setting was turned off in achieving this. Table 4 presents the four mesh resolutions obtained using equation (9). In investigating the effects of these minimum cell sizes on convergence, comparison of measured and predicted liquid length of WCO at 100 MPa is presented in Fig. 2. With time, the experimental spray liquid length increases until a quasi-steady length was attained. Similar observations occurred in the predicted spray liquid length at all mesh resolutions. Furthermore, it can be observed that coarser grids of 0.5 and 1 mm over predicted the spray liquid length up to the timing of 0.74

ms ASOI when compared to the finer grids of 0.25 and 0.125 mm. There is no significant difference between the convergence of the predicted liquid length for both mesh resolutions of 0.25 and 0.125mm up to the timing of 0.7 ms ASOI. By considering spray propagation period towards the end of injection, spray liquid length exhibits grid convergence with better accuracy when the mesh resolution is 0.25 mm. Based on these findings, the mesh resolution of 0.25 mm with embedded scale of 3 was considered optimum for simulation activities and resolving flow fields especially at the injector nozzle boundary. Similar mesh resolution of 0.25 mm was obtained in previous study by [31].

3.2 Evaporating Spray

The evolution of the simulated and experimental evaporating sprays at 1.5 ms ASOI i.e. 0 ms AEOI (after end of injection)) are presented in Fig. 3 using temperature contours. The vapor phase lengths were not captured in the experiment since the Mie scattering technique was only used. As described in [18], simulated liquid length is defined by an axial position that encompassed 95% of the injected fuel mass at a given time from the start of injection. In Fig. 3, the liquid part of the vaporizing spray is defined by blue color (part identified with broken line) of the temperature contour images having considered the fuel distillation temperatures, which is around 600 K. As shown in Fig. 3, the simulated liquid lengths have similar structure/shape that were observed in the experiment (grey images). As injection pressure increased, the liquid phase length became shorter while the vapor phase length penetrated further. These observations suggest that atomization was enhanced leading to formation of fine droplets as injection pressure increased. As injection pressure increased, spray momentum increased which further led to fine droplets propagating further downstream. As fine droplets propagate through hot quiescent air, surface evaporation and momentum of air entrained into the spray were enhanced leading to shorter liquid and longer vapor phase lengths. Figure 4 presents the temporal variation of the simulated and experimental

vaporizing sprays. It could be observed that the simulated liquid phase length followed similar trend obtained in the experiment. As discussed earlier, for both simulated and experimental data, after an initial development period, the tip of the liquid phase fuel region reached a steady condition and fluctuated about a mean axial location because of turbulence. At all injection pressures, both WCO and its surrogate produced longer liquid phase length compared to diesel. This can be attributed to inferior atomization by WCO, which limited the rate of evaporation as smaller quantity of air entrained in the spray. In addition, higher boiling point of WCO characterized by the fuel distillation temperature, T-90 and low volatility, could have initiated longer liquid phase length. This phenomenon has been observed in previous works on liquid phase penetration length [33-34]. In order to gain insight on the effect of injection pressure and physical properties on the spray droplet sizes, temporal variations of sauter mean diameter (SMD) are presented in the supplementary material. Furthermore, the effect of injection pressure on mixing in terms of axial spatial distributions of the turbulent kinetic energy are also reported in the supplementary material.

3.3 Combustion Characteristics

3.3.1 Flame structures, interactions with spray and intermediate species

Figure 5 presents contours of WCO, diesel and their surrogates flame structures during the auto-ignition stage. The simulated flame structures were obtained using the hydroxyl radical (OH*) contour since it is a good marker of high temperature and heat release flame regions. The major kinetic path for forming OH* in non-premixed flames is the exothermic reaction; $CH+O_2 \rightarrow CO+OH^*$ [28]. Once formed, the OH* returns rapidly to its ground state through chemiluminescent emission and collisional quenching. Temperature contours were used to describe the spray-flame interactions. Stoichiometric lines (i.e. at equivalence ratio, $\phi = 1$ with black broken line) were embedded on the contours to define mixture regions where flame occurred. Outside the line, the mixture is considered lean while it is rich if inside. For

comparisons, line of sight OH* images of the reacting sprays from experiment were used. Images of the liquid part of the experimental liquid lengths at the time of auto-ignition were superimposed on the flame images in order to investigate spray flame interactions. It can be observed that auto-ignition spots with high temperature part appeared inside the stoichiometric line where the mixture is rich. This observation is in line with the study reported in [35], where vapor fuel and air premixed to form a rich mixture prior to auto ignition. As injection pressure increased up to ultra-high value of 300 MPa, the spray velocity increased pushing the auto-ignited reaction zones further downstream towards the lean side of the mixture space. The simulated auto-ignition flame structures suggests that OH* species were formed at the edge of the spray very close to the stoichiometric line while they were pushed further downstream (towards stoichiometry conditions) as injection pressure increased. It can be observed that the simulated OH* is concentrated at the periphery of the fuel vapor (high temperature region). This information further shed more light on the OH* experimental images obtained through the line of sight technique. The locations of the auto-ignited flame structures are very close to the line of sight images. Both simulated and experimental results showed that WCO auto-ignition locations measured from the injector nozzle tip were shorter compared to diesel fuel at all injection pressures. Since the auto-ignition locations of the WCO biodiesel flame were shorter, as depicted in the temperature contour images, there were more spray flame interactions. Furthermore, the simulated ignition delay times (inset of contour images) followed similar trend obtained in the experiment. As injection pressure increased from 100 to 300 MPa, simulated and experimental ignition delays were shortened signifying fuel-air mixing enhancement and accelerated rate of reaction. Irrespective of injection pressures, WCO ignition delays were shorter for both simulated and experimental data. The main contributing factor for shorter ignition delay in WCO is the higher cetane number presented in table 3. While many

chemical reactions occur during ignition of fuels [36], the temporal variation of the simulated formaldehyde, CH_2O and OH* species with iso-surface images are presented in Fig. 6. Furthermore, temperature and rate of heat release data associated with the species formed are also presented. CH_2O species has been found to characterize flames at low temperature and initial fuel-rich premixed reaction region [37]. In Fig. 6, the formation of CH_2O species preceded the evolution of OH* species. The appearance of CH_2O prior to OH* species indicates early occurrence of the first stage of ignition with low temperature heat release (LTHR) accompanied with cool flame depicted by the blue iso-surface. Furthermore, during the formation of the cool flame, the reaction paths of CH_2O with O_2 forming other intermediate products has been reported to be highly sensitive to the formation of OH* species [38]. CH_2O species is usually formed during the decomposition of ketohydroperoxides, which are the result of a complex low temperature oxidation mechanism. Figure 7 provides more information about the evolution of CH_2O during the first stage ignition at a temperature higher than the ambient i.e. 885 K. It can be observed that the first stage ignition occurred outside the stoichiometric line i.e. lean mixture space. In Fig. 6, with time, as the fuel (green iso-surface) is consumed through oxidation, CH_2O species increased in quantity and size, reaching a peak value. CH_2O later decreased in quantity after being consumed during oxidation processes forming OH* species. The formation of OH* species characterized auto-ignition (flame kernel depicted with red iso-surface) with high temperature heat release. In Fig. 6, simulated data followed similar trend with the experiment confirming an earlier appearance of OH* in WCO and its surrogates compared to diesel. As injection pressure increased to 300 MPa, there was enhancement in mixing and vaporization which further led to faster reactions thus making both CH_2O and OH* time scales. Furthermore, the quantities of CH_2O and OH* species increased due to enhancement in mixing as fuel injection pressure increased to 300 MPa. By comparing the two fuels, the peak values of

CH_2O and OH* species in WCO were lower compared to diesel. The lower peak values of CH_2O and OH* could be due to inferior atomization qualities of WCO leading to less entrained air in the mixture. At an early stage, the quantities of the CH_2O and OH* produced by WCO were higher compared to diesel. Furthermore as injection pressure increased to 300 MPa, OH* declined faster due to WCO reactivity (higher cetane number) and mixing enhancement. For both fuels increase in injection pressure led to increase in heat release rate (HRR) with no significant difference in flame temperatures. After autoignition, in Fig. 8, during the fuel injection period, flame size increased and became quasi-steady at a location known as the flame lift-off (indicated by broken lines). The distance measured from the injector to the quasi-steady location of the lifted flame is referred to as the flame lift-off length. Upstream of the lifted flame, the air entrained plays a vital role in soot formation processes in diesel engine. Details on the analyses of air entrained upstream of the lifted flame are presented in the supplementary material using empirical equations by [39]. In Fig. 8, the region downstream of the flame lift-off is characterized by a non-premixed zone represented by the OH* species contour. This non-premixed zone, which depends on the air entrained upstream, is usually formed at the periphery of the diffusion flame [40]. By adopting the method in [41], simulated flame lift-off length was defined as the first axial location of the Favre-averaged OH* mass fraction reaching 2% of its maximum in the computational domain. As injection pressure increased, spray velocity increased thus making the flame to be further pushed downstream towards the lean side in the mixture space. However, the flame moved upstream towards the rich mixture location for stabilization.. In Fig. 8, OH* species was observed to be more concentrated downstream at the vaporized spray edge especially at the stoichiometric region where the flame is in close proximity to the oxidant. In the lifted flame, OH* mass fraction increased as injection pressure increased. This implies that an increase in injection pressure produced more fine droplets enhancing more air

(O_2 part) to be entrained leading to the production of more OH* species in the flame. Since diesel vaporized better than WCO, it produced higher OH* mass fraction along the stoichiometric mixture line. The peripheral structures of the simulated OH* flame are similar to the line of sight images with both flames converging towards the upstream location of the injector. Both experimental and simulated flame structures tend to converge upstream in WCO and this in turn led to shorter lift-off length compared to diesel. Furthermore, considering the temperature contour image, WCO displayed more spray-flame interactions as compared to diesel. In terms of spray-flame interactions, the simulated data captured similar trend displayed by the experimental data except for diesel at 100 MPa. At all injection pressures, the simulated data followed similar trends in the experiments with WCO flame lift –off lengths shorter compared to diesel. Several factors have been reported to have effect on lift-off stabilization of diesel engine flames [42-43]. It was observed that there was no direct correlation between high temperature ignition delay and lift length [43]. However, it was reported that flame lift –off stabilization occurred when fuel–air mixture approaching the lift-off position of the jet mixes with hot combustion products triggering auto-ignition at low temperature conditions [44]. It was further observed that a cool flame at low temperature conditions usually exists upstream of the high temperature stabilized lifted flame [42]. A cool flame is an indication that ignition processes at low temperature are continuously occurring within the fuel jet as fuel and ambient air mix upstream of the lifted flame. Furthermore, the transition from cool flame to high temperature combustion at the lift-off length depends strongly on the fuel type [42]. Therefore, in clarifying lift off stabilization of WCO against diesel, the locations of the CH_2O and OH* species are presented by iso-surface contour images earlier described in Fig. 6 (see inset of the graphs). In Fig. 6, for both fuels, it could be inferred that a cool flame with low temperature characterized by CH_2O species exists upstream while the high temperature flame characterized by OH* species is lifted and

stabilized downstream. The spatial variations of CH_2O and OH* species are presented in in Fig. 9. While the quantity of CH_2O produced by WCO was less compared to diesel irrespective of injection pressure, it covered smaller areas compared to diesel surrogate (refer to Fig.6). Due to the location of CH_2O species, WCO hot flames tends to propagate more upward towards the injector location compared to diesel. During the fuel injection period, as more hot air was entrained upstream, it mixes with cool flame leading to the occurrence of high temperature ignition. The downstream high temperature flame propagated upward joining the new flame upstream leading to a quasi-stable flame to be formed. Further information in Fig. 9 showed that irrespective of injection pressure, at an axial location the destruction of CH_2O species led to the formation of OH* species . In addition, it can be observed that as injection pressure increased, mixing was enhanced which favoured the conversion of CH_2O to OH* species as temperature increased. In Fig. 9, both CH_2O and OH* species reaction zones moved further downstream as injection pressure increased. In Fig. 10 at 0.25ms AEOI, the flame further propagated upward towards the injector and stretched radially in all directions. Both simulated and experimental OH* images exhibited flames with parts converging more upstream compared to the lifted flames presented in Fig. 8. The high level of convergence towards the injector tip could be due to flame propagation towards the richer mixture region after the end of injection. As observed earlier, WCO flames converged more after the end of injection event.

3.3.2 Temperature – equivalence ratio ($T - \phi$) map

In order to investigate the effect of mixture formation on auto-ignition and subsequent combustion events, scattered plots of temperature were plotted against equivalence ratio. Further post processing and analyses carried on contour images for the first stage ignition images in Fig. 6 yielded the $T - \phi$ maps in Fig. 11. In Fig.11, it can be observed that at all injection pressures, the scattered plots converged from low to high equivalence ratio regions

as temperature decreased. As described earlier in section 3.2, the sudden increase in temperature above the ambient conditions (i.e. 885 K), reaching peak values at a region close to $\phi < 1$ is an indication of the first stage ignition. Due to enhancement in mixing, it could be observed that there was an early occurrence of the first stage of ignition as injection pressure increased to ultra-high value of 300 MPa. Furthermore, the first stage of ignition occurred earlier in WCO. Quantitative analyses of the temperature-equivalence ratio maps for the main ignition, lifted flames during and after end of fuel injection events are presented in the supplementary material.

3.3.3 Emission modeling

In gaining detailed understanding on soot characteristics of the fuels, C_2H_2 contours of the simulated flames with the KL images obtained from the two-color pyrometry experiments are presented in Fig. 12. The soot KL factor is expressed in soot number per cm^2 where K is the soot absorption coefficient expressed as soot number per cm^3 while L is the path length in cm. C_2H_2 species has been found to be a precursor for soot formation. It constitutes the building block for the Polycyclic Aromatic Hydrocarbon (PAH) mechanism, which is important for soot formation [41]. It can be observed in Fig. 12, that as injection pressure increased from 100 to 300 MPa, the trend in simulated soot formed compared well with experiment. Furthermore, as injection pressure increases, there was decrease in the soot area while the quantity of soot reduced spatially. These could be attributed to mixing enhancement leading to more air entrained upstream of the combusting zone. Irrespective of injection pressures, soot is formed within the rich region of the mixture space. This observation is in accordance to the Dec's conceptual model [40] for conventional diesel combustion processes. As observed in section 3.3.1, at the stoichiometric line, higher concentration of OH* had a great influence on the soot formation processes. Hence, as injection pressure increased, OH* increased with significant enhancement in oxidation leading to less soot quantify being

formed. It was also observed that WCO equivalence ratios were higher during ignition and quasi steady state signifying less air entrainment in flames (refer to supplementary material). However, in Fig. 12 the contour intensity of WCO biodiesel were lower compared to diesel. This could imply that WCO soot formation does not depend on the quantity of air entrained. Figure 13 presents the temporal variation of the soot quantity formed by WCO and diesel fuels. It can be observed that both simulated and experimental results showed that soot quantity attained a peak after the end of injection event. While the simulated soot in WCO flame appeared early, considering the effect of injection pressures, its temporal variations followed similar trends like the experiment. For diesel, similar trends could be observed for both simulated and experimental soot formed considering injection pressures conditions. Compared to WCO, in diesel, the simulated data tend to agree more with experimental data especially at higher injection pressures of 200 and 300 MPa respectively. Deviations in the simulated data compared to experiments especially for WCO could be attributed to the type of soot model used in this study. A good agreement between the experiment and simulated soot data needs to be worked at in the future. This could involve the use of detailed soot models capable of solving complex soot formation and oxidation with detailed chemistry. Decline in the net soot formed can be attributed to enhancement in oxidation as injection pressure increased. Soot quantity increased from the beginning of the combustion event towards the end of injection (1.5 ms ASOI). However, as time approaches the end of the combustion event i.e. after end of fuel injections the soot formed decreased due to enhancement in oxidation. WCO displayed early soot formation and produced more soot compared to diesel towards the EOI. However at a later period i.e.1.75ms ASOI (0.25 ms AEOI), at all injection pressures, the net soot formed by WCO declined faster compared to diesel. Since WCO entrained less air compared to diesel, the reduction in net soot at a latter period beyond EOI could be attributed significantly to the chemical bounded fuel oxygen.

McCormick and co-workers [45] suggested that biodiesel has tendency to provide oxygen in its spray molecules during combustion processes thereby enhancing soot oxidation. As presented in Table 3, oxygen content in WCO is 11.1% as against diesel which is less than 1% or negligible. Therefore, as injection pressure increased, the oxygen atom in WCO could have enhanced soot oxidation during the combustion events.

4. Conclusions

Numerical investigations based on the RNG k- ε turbulent model were carried out to investigate the effect of ultra-high injection pressure on spray combustion processes of WCO and diesel Fuels. Investigations on the role of mixture formation on combustion and stabilizing mechanism of lifted flame were also investigated. The results obtained in this study are summarized as follows.

i. The simulated liquid length captured the trend observed in experiment. Increase in injection up to ultra-high value enhanced atomization leading to decrease in spray liquid length with increase in vapor length. Longer spray liquid length was produced by WCO as a result of inferior atomization.

ii. Prior to the main ignition, a first stage ignition with low temperature heat release characterized by CH_2O species was observed. The main ignition events (second stage ignition) occurred at high temperature condition with the formation of OH*species.

iii. There was a good agreement between the simulated and experimental ignition delays. Increase in injection up to 300MPa led to increase in the rate of reaction, which further resulted in shorter ignition delays for both fuels. While ignition took place at the rich mixture space, its locations were pushed downstream towards the

stoichiometry mixture line as injection pressure increased. WCO had shorter ignition delay and faster reactivity.

iv. The simulated flame lift-off length for both fuels compared well with experiment. Increase in injection pressure pushed the stabilized flame region further downstream leading to longer-lift off length. An upstream cool flame characterized by the CH_2O species enhanced the formation of a stabilized lifted flame downstream. WCO had shorter flame lift-off length with less air entrainment.

v. Both simulated and experimental results showed that as injection pressure increased, less interaction between spray and flames occurred. In comparison with diesel, more spray flame interactions occurred in WCO irrespective of injection pressure conditions.

vi. As injection pressure increased, there was increase in the rate of heat release. As compared to diesel, low and high temperature heat release occurred earlier in WCO.

vii. The net soot formed decreased as injection pressure increased. Compared to diesel, the oxygen atom in WCO molecules played a vital role in soot formation.

5. Acknowledgements

The authors will like to thank the KAUST high performance computing (HPC) laboratory for their assistance in using many computer CPUs for the simulation activities.

Nomenclature

C_μ	Model constant for fluid flow (= 0.22)
P	Pressure of gas mixture [Pa]
S_{ij}	Strain rate tensor [m^2/s^2]
u	Gas velocity [m/s]
δ	Kronecker delta
ε	Dissipation of kinetic energy

k	Sub-grid turbulent kinetic energy [m^2/s^2]
μ	Dynamic Viscosity [Pa.s]
μ_t	Turbulent viscosity [Pa.s]
ϕ	Equivalence ratio
ρ	Density of the gas mixture [kg/m3]
τ_{ij}	Reynold stress sub-grid scale tensor [m^2/s^2]

Abbreviation

ASOI	After start of injection
AEOI	After end of Injection
RANS	Reynolds-averaged Navier-Stokes
T-90	Temperature at which 90 % volume of fuel has vaporised
WCO	Waste Cooking Oil Biodiesel
RNG	Renormalization Group Theory

References

[1] The Role of Biofuels Beyond 2020 Commissioned by BP Executive summary 2013:1–30.

[2] Zhu J, Nishida K, Kuti OA, Moon S. Quantitative analyses of fuel spray-ambient gas interaction by means of LIF-PIV technique. Atomization and Sprays 2011;21:447–65.

[3] Zhu J, Kuti OA., Nishida K. An investigation of the effects of fuel injection pressure, ambient gas density and nozzle hole diameter on surrounding gas flow of a single diesel spray by the laser-induced fluorescence-particle image velocimetry technique. Int J Engine Res. 2012;14:630–45.

[4] Kuti OA, Nishida K, Zhu J. Experimental studies on spray and gas entrainment characteristics of biodiesel fuel: Implications of gas entrained and fuel oxygen content on soot formation. Energy 2013;57:434–42.

[5] Kuti OA, Zhu J, Nishida K, Wang X, Huang Z. Characterization of spray and combustion processes of biodiesel fuel injected by diesel engine common rail system. Fuel 2013;104:838–46.

[6] Jin C, Yao M, Liu H, Lee CF, Ji J. Progress in the production and application of n-

butanol as a biofuel. Renew Sustain Energy Rev 2011;15:4080–106.

[7] Zhang W, Nishida K, Gao J, Miura D. An experimental study on flat-wall-impinging spray of microhole nozzles under ultra-high injection pressures Proc IMechE Part D J. Automob. Eng. 2008; 222: 1731-41.

[8] Tao F, Bergstand P. Effect of Ultra-High Injection Pressure on Diesel Ignition and Flame under High-Boost Conditions. SAE Paper 2008-01-1603, 2008.

[9] Nishida K, Zhang W, Manabe T. Effects of micro-hole and ultra-high injection pressure on mixture properties of D.I. diesel spray. SAE Paper 2007-01-1890, 2007.

[10] Minato A, Tanaka T, Nishimura T. Investigation of premixed lean diesel combustion with ultra-high pressure injection. SAE Paper 2005-01-0914; 2005.

[11] Hull A, Golubkov I, Kronberg B, van Stam J. Alternative Fuel for a Standard Diesel Engine. Int J Engine Res. 2006; 7:51−63.

[12] Ozsezen AN, Canakci M, Sayin C. Effects of biodiesel from used frying palm oil on the performance, injection, and combustion characteristics of an indirect injection diesel engine. Energy Fuels 2008; 22:1297−1305.

[13] Lapuerta M, Rodríguez-Fernandez J, Agudelo JR. Diesel particulate emissions from used cooking oil biodiesel. Bioresour. Technol. 2008; 99:731−40.

[14] Muralidharan K, Vasudevan D. Performance, emission and combustion characteristics of a variable compression ratio engine using methyl esters of waste cooking oil and diesel blends. Appl. Energy 2011; 88: 3959−68.

[15] Hwang J, Jung Y, Bae C. Spray and combustion of waste cooking oil biodiesel in a compression-ignition engine. Int J Engine Res 2015;16:664−79.

[16] Hwang J, Bae C, Gupta T. Application of waste cooking oil (WCO) biodiesel in a compression ignition engine. Fuel 2016;176:20–31.

[17] Zhong W, Tamilselvan P, Wang Q, He Z, Feng H, Yu X. Experimental study of spray characteristics of diesel/hydrogenated catalytic biodiesel blended fuels under inert and reacting conditions. Energy 2018;153:349–58.

[18] Richards KJ, Senecal PK, Pomraning E. CONVERGE (v2.3), Convergent Science, Inc., Madison, WI (2016).

[19] Som S, Senecal PK, Pomraning E. Comparison of RANS and LES Turbulence Models against Constant Volume Diesel Experiments. ILASS Americas, 224th Annual Conference on Liquid Atomization and Spray Systems, San Antonio, TX, May 2012.

[20] Xue Q, Som S, Senecal PK, Pomraning E. A study of grid resolution and SGS models for LES under non-reacting spray conditions. ILASS Americas, 25th Annual Conference on Liquid Atomization and Spray Systems, Pittsburgh, PA, May 2013.

[21] Reitz RD, Diwakar R. Structure of high-pressure fuel sprays. SAE Paper 870598, 1987.

[22] Senecal PK, Richards KJ, Pomraning E, Yang T, Dai MZ, McDavid RM, Patterson MA, Hou S, Shethaji T. A new parallel cut-cell cartesian CFD code for rapid grid generation applied to in-cylinder diesel engine simulations. SAE 2007-01-0159, 2007.

[23] Schmidt DP, Rutland CJ. A new droplet collision algorithm. J Comp. Phys 2000;, 164: 62-80.

[24] Post SL, Abraham J. Modeling the outcome of drop-drop collisions in diesel sprays. Int. J of Multiphase Flow 2002; 28:997-1019.

[25] Kuti O, Nishida K, Sarathy M, Zhu J. Fuel spray combustion of waste cooking oil and palm oil biodiesel: direct photography and detailed chemical kinetics. SAE Paper 2013-01-2554, 2013.

[26] Herbinet O, Pitz WJ, Westbrook CK. Detailed chemical kinetic mechanism for the oxidation of biodiesel fuels blend surrogate. Combust Flame 2010; 157:893-908.

[27] Zhaoyu L, Plomer M, Lu T , Som S, Longman DE, Sarathy SM, Pitz JW. A reduced mechanism for biodiesel surrogates for compression ignition engine applications. Fuel 2012; 99:143-153.

[28] Kathrotia T. Reaction kinetics modeling of oh*, ch*, and c_2* chemiluminescence, Ph.D Dissertation, University of Heidelberg, 2011.

[29] Hiroyasu H, Kadota T. Models for combustion and formation of nitric oxide and soot in direct injection diesel engines. SAE Paper 760129, 1976.

[30] Nagle J, Strickland-Constable RF. Oxidation of carbon between 1000-2000 ^{o}C. Proceedings of the Fifth Carbon Conference 1962; 1: 154-164.

[31] Senecal PK, E Pomraning, Richard KJ, Som S. Grid-convergent spray models for internal combustion engine CFD simulations. ASME Paper, ICEF2012-92043, 2012.

[32] Kuti OA, Sarathy M, Nishida K, Roberts W. Numerical studies of spray combustion processes of palm oil biodiesel and diesel fuels using reduced chemical kinetic mechanisms. SAE Paper 2014-01-1143, 2014.

[33] Fang T, Lin Y-C, Fong TM, Lee C-F. Biodiesel combustion in an optical hsdi diesel engine under low load premixed combustion conditions. Fuel 88(2009):2154-62.

[34] Siebers D. Liquid-phase fuel penetration in diesel sprays. SAE Paper 980809, 1998.

[35] Venugopal R, Abraham J. A 2-D DNS investigation of extinction and reignition dynamics in non-premixed flame–vortex interactions .Combust Flame 2008; 153:442-64.

[36] Sarathy SM, Westbrook CK, Mehl M, Pitz WJ, Togbe C, Dagaut P , Wang H, Oehlschlaeger MA, Niemann U, Seshadri K, Veloo PS, Ji C, Egolfopoulos FN, Lu T. Comprehensive chemical kinetic modeling of the oxidation of 2-methylalkanes from C_7 to C_{20}. Combust. Flame 2011; 158: 2338–57.

[37] Alfazazi A, Kuti OA, Naser N, Chung SH, Sarathy M., Two-stage Lagrangian modeling of ignition processes in ignition quality tester and constant volume combustion chambers. Fuel 2016; 185:589–98.

[38] Vasudevan V, Davidson DF, Hanson R, Bowman TC, Golden DM. High-temperature measurements of the rates of the reactions $CH_2O + Ar \rightarrow$ Products and $CH_2O + O_2 \rightarrow$ Products. Proc. Combust. Inst 2007; 31:175-183.

[39] Naber J, Siebers D. Effects of gas density and vaporization on penetration and dispersion of diesel sprays. SAE Paper 960034, 1996.

[40] Dec JA. Conceptual Model of di diesel combustion based on laser-sheet imaging*. SAE Paper 970873, 1997.

[41] Wang H, Reitz RD, Yao M, Yang B, Jiao Q, Qiu L. Development of an n-heptane-n-butanol-PAH mechanism and its application for combustion and soot prediction," Combust Flame 2013; 160 :504-19.

[42] Pickett LM, Siebers D, Idicheria C. Relationship between ignition processes and the lift-off length of diesel fuel jets. SAE Paper 2005-01-3843, 2005.

[43] Persson H, Andersson O, Egnell R. Fuel effects on flame lift-off under diesel conditions. Combust Flame 2010; 158: 91-7.

[44] Pei Y, Som S, Pomraning E, Senecal PK, Skeen SA, Manin J, Pickett LM. Large eddy simulation of a reacting spray flame with multiple realizations under compression ignition engine conditions. Combust Flame 2015; 162:4442-55

[45] McCormick RL, Graboski MS, Alleman TL, Herring AM. Impact of biodiesel source material and chemical structure on emissions of criteria pollutants from a heavy-duty engine. Environ.Sci.Technol 2001; 35:1742-1747.

Table

Table 1 Breakdown of the WCO surrogate formulation from biodiesel major components

Biodiesel major component	**Biodiesel major component mass fraction**	**Approximate resulting mixtures based on the surrogates**	**Tri-surrogate mass fraction**		
			nC_7H_{16} (*n*-heptane	$C_{11}H_{22}O_2$ (methyl decanoate)	$C_{11}H_{20}O_2$ (methyl-9-decenoate)
Methyl Palmitate ($C_{17}H_{34}O_2$)	0.085	$0.8C_7H_{16}$+ $C_{11}H_{22}O_2$	$\frac{0.8}{1.8} * 0.085$	$\frac{1}{1.8} * 0.085$	-
Methyl Stearate ($C_{19}H_{38}O_2$)	0.029	$1.2C_7H_{16}$+ $C_{11}H_{22}O_2$	$\frac{1.2}{2.2} * 0.029$	$\frac{1}{2.2} * 0.029$	
Methyl Oleate ($C_{19}H_{36}O_2$)	0.428	$1.1C_7H_{16}$+ $C_{11}H_{20}O_2$	$\frac{1.1}{2.1} * 0.428$		$\frac{1}{2.1} * 0.428$
Methyl Linoleate ($C_{19}H_{34}O_2$)	0.355	$1.05C_7H_{16}$+ $C_{11}H_{20}O_2$	$\frac{1.05}{2.05} * 0.355$		$\frac{1}{2.05} * 0.355$
Methyl Linolenate ($C_{19}H_{32}O_2$)	0.103	C_7H_{16}+ $C_{11}H_{20}O_2$	$\frac{1}{2} * 0.103$		$\frac{1}{2} * 0.103$
		Total	0.511=51.1%	0.0604=6.04%	0.4286=42.86%

NB: Each surrogate component mass fraction from the relation;

$$\frac{mole\ of\ surrogate\ in\ the\ resulting\ mixture}{Total\ mole\ of\ resulting\ surrogate\ mixture} * mass\ fraction\ of\ major\ biodiesel\ component$$

Table 2 Summary of the parameters for simulation

Break-up	KH-RT
Droplet evaporation	Frossling correlation
Droplet collision	No time counter (NTC) algorithm
Kinetic modelling	SAGE chemical kinetic solver
Mechanism	Lu et al. (2012)
Fuel	Surrogates
Diesel	nC7H16 (chemical), $C_{14}H_{30}$(physical)
Waste Cooked Oil Biodiesel	$C_{11}H_{22}O_2$ (**6.04%**), $C_{11}H_{20}O_2$ (**42.9%**), nC_7H_{16}(**51.1%**)
Soot formation	Hiroyasu-NSC soot model
Simulation period	1.5 ms(Spray), 2.2 ms (Combustion)
Time step	$1*10^{-5}$ sec (maximum), $1*10^{-11}$ sec (minimum)
Ambient conditions	
Density (kg/m^3)	15 (-10^o ATDC)
Pressure (MPa)	4.0
Temperature (K)	885
Injection conditions	
Nozzle diameter (mm)	0.16
Fuel pressure (MPa)	100, 200 and 300
Duration	1.5ms

Table 3 Properties of fuels used in experiments [5]

Fuel Property	WCO	Diesel
Density @ 15^{o}C (kg/m^{3})	885	830
Viscosity @ 40^{o}C (mm^{2}/s)	4.45	3.36
Surface tension @ 20^{o}C (mN/m)	33.1	30.6
Cetane number	51	45
Distillation temperature (^{o}C)	360	320
Heating value (MJ/kg)	39.03	43.1
Sulphur content (ppm)	<3	<19
Carbon content (wt. %)	77.9	86.1
Hydrogen content (wt. %)	12.0	13.8
Oxygen content (wt. %)	10.1	<1

Table 4 AMR embed scales and minimum cell from equation (9), $dx_{base} = 2mm$

Embedding Scale	Minimum Cell Size (mm)
1	1.0
2	0.5
3	0.25
4	0.125

Figure

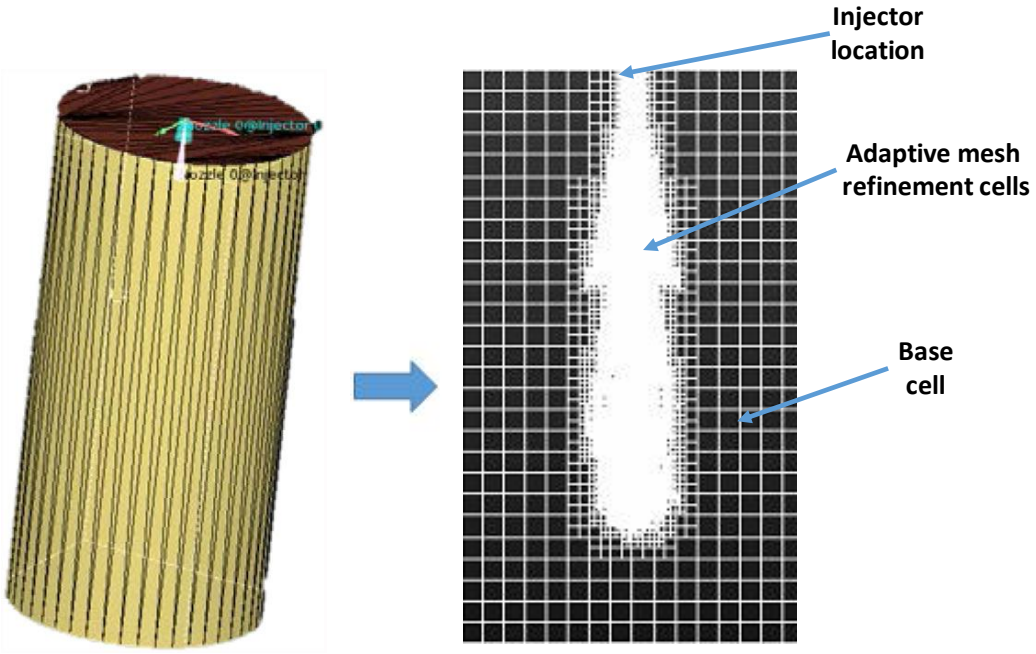

Figure 1 Constant volume chamber profile used for generating grid during CONVERGE runtime (left). Cartesian grid generated during CONVERGE runtime (right).

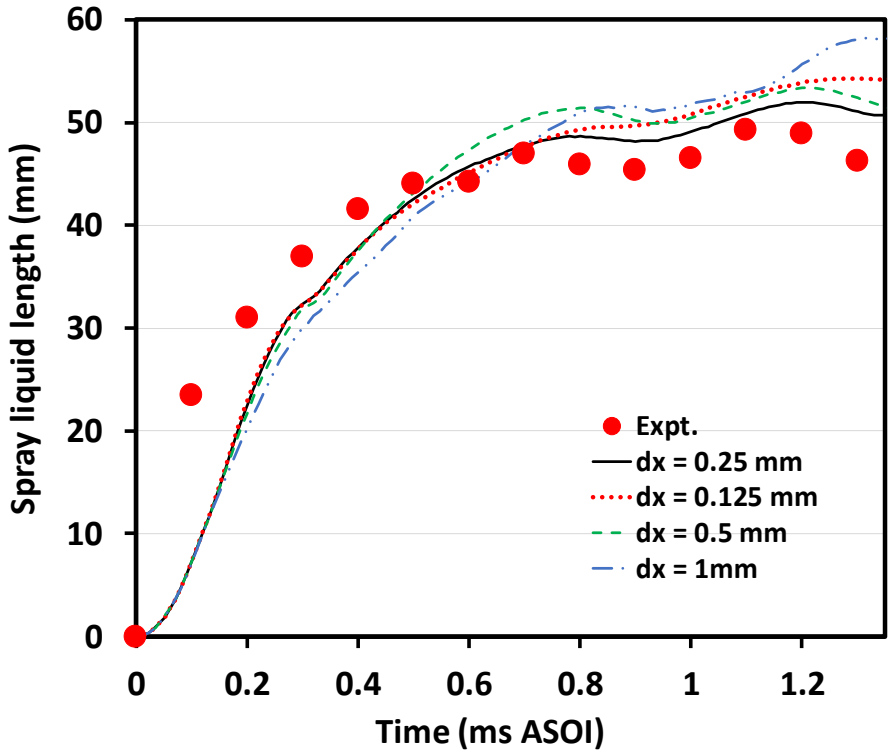

Figure 2 Comparison of experimental and predicted spray liquid length for the WCO evaporating sprays at 100 MPa. Four predicted curves are presented for the cell sizes presented in Table 1.

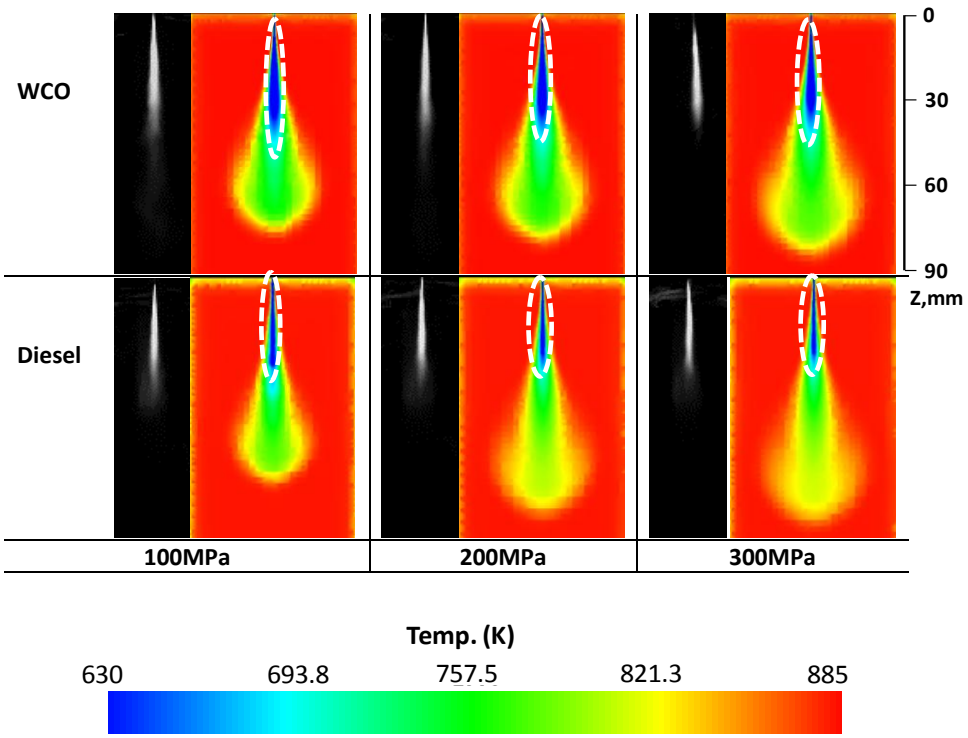

Figure 3 Variation of evaporating sprays with injection pressure, at time, t = 1.5ms ASOI. Experimental evaporating spray are in grey (left) while simulated evaporating spray are depicted by contour images (right). White broken lines on simulated images indicate the liquid length (blue) of evaporating spray.

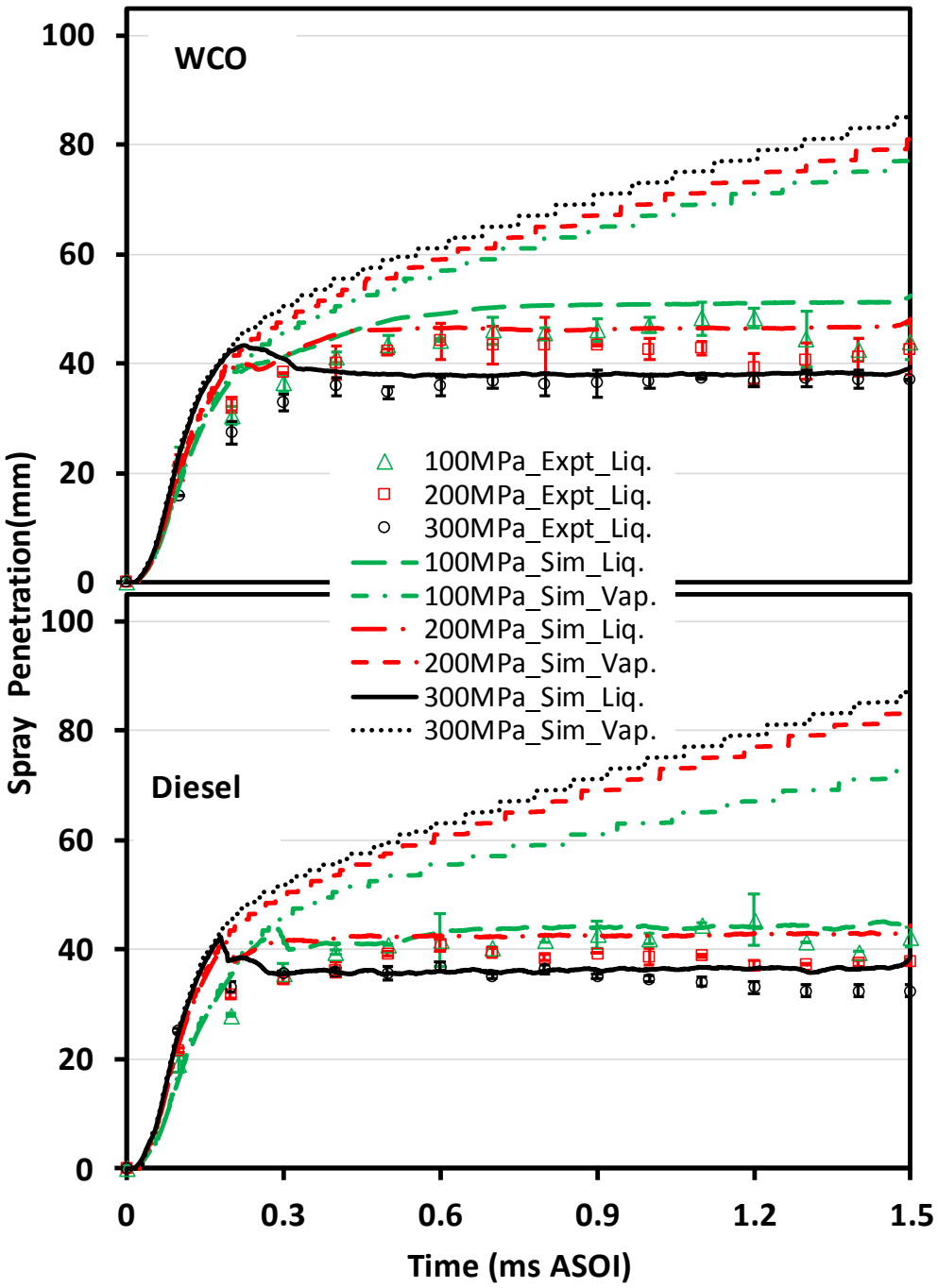

Figure 4 Temporal variation of predicted evaporating spray penetration with injection pressure validated with experiment

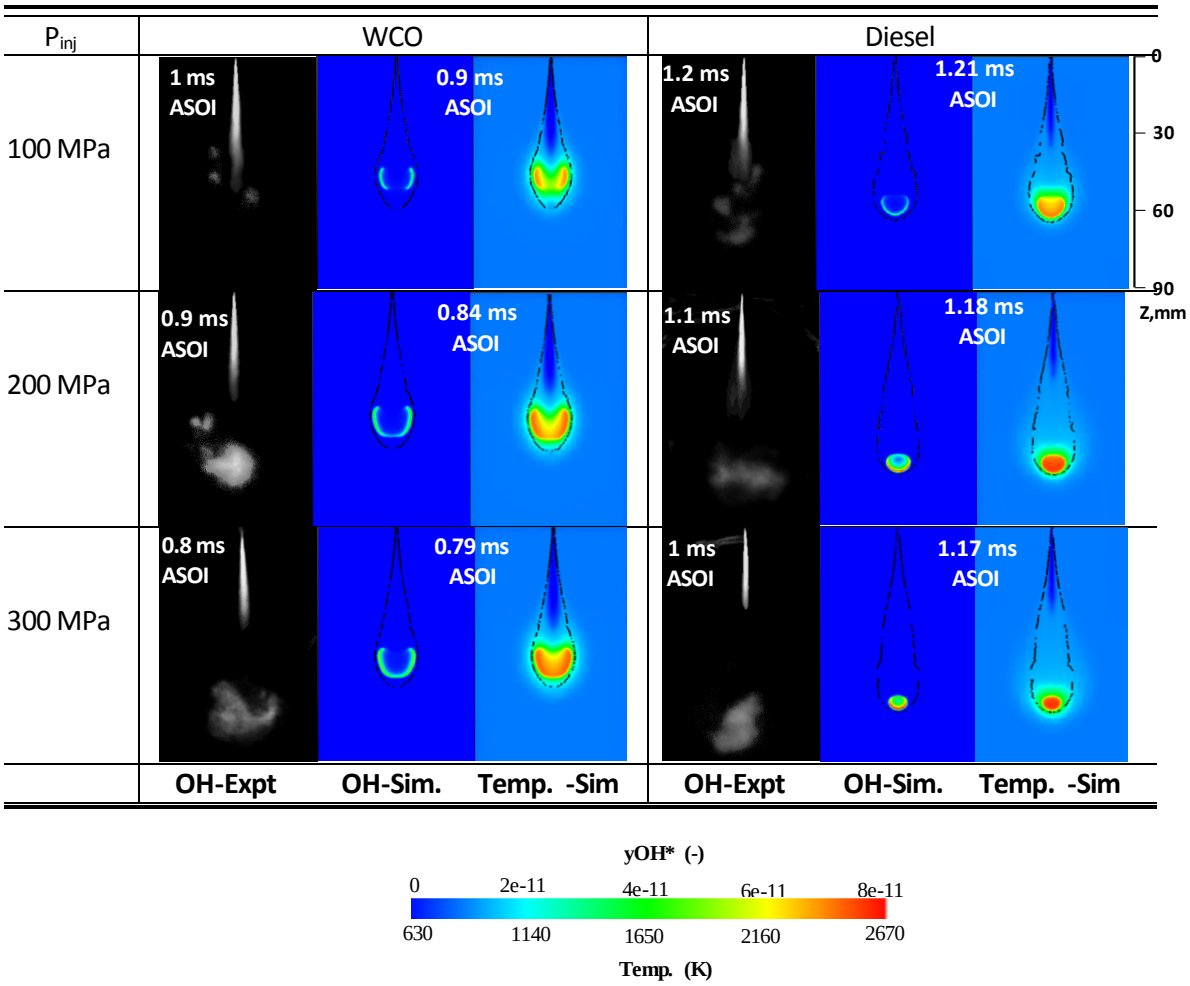

Figure 5 Variation of ignition delay with injection pressure. Experimental ignition delay images are in grey (left) while simulated ignition are depicted by contour images (right). Black broken lines on contour images depict stoichiometry line.

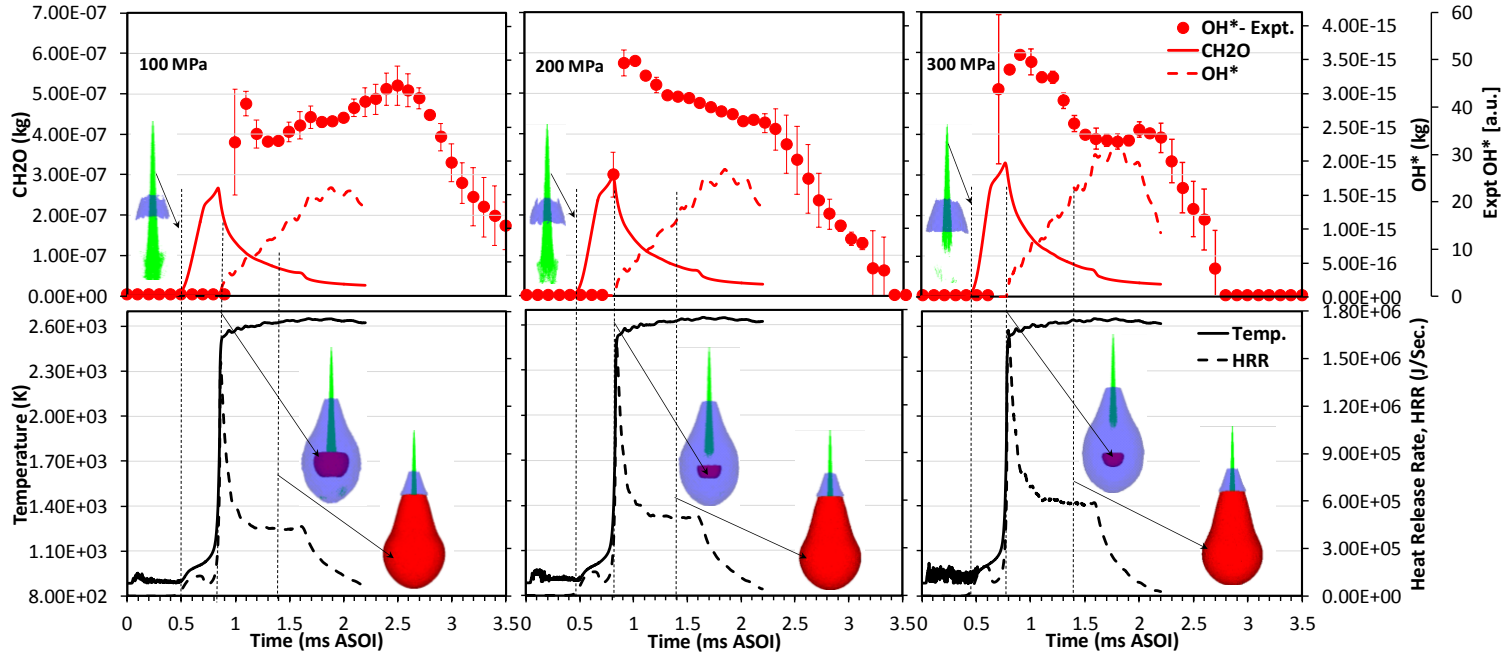

(a)

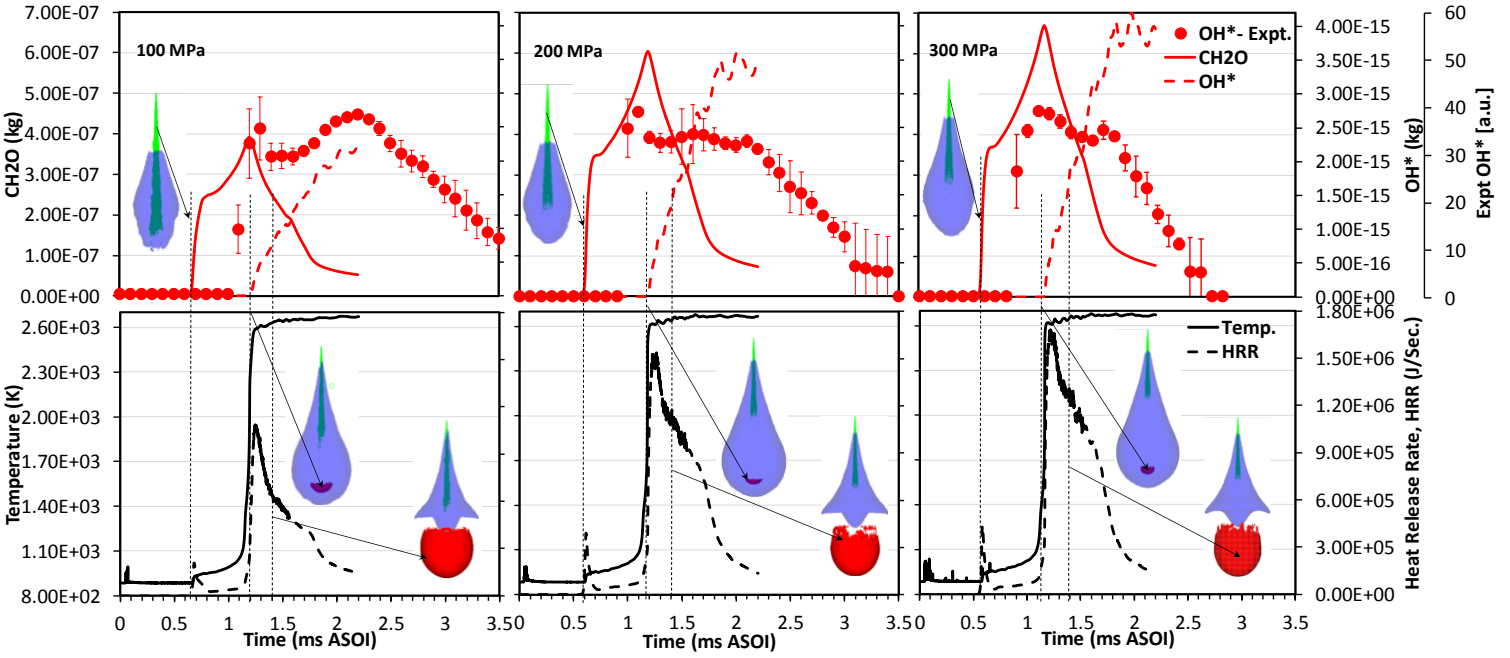

(b)

Fuel CH_2O OH*

Figure 6 Temporal variations of predicted and experimental CH_2O and OH*species data with injection pressure (a) WCO (b) Diesel

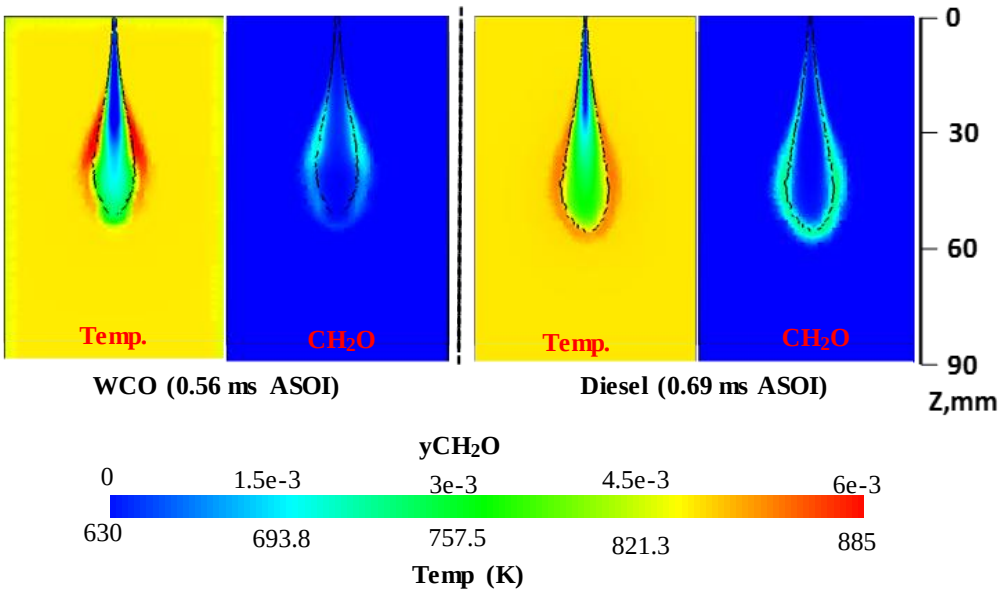

Figure 7 Evolution of CH_2O and flame temperature during first stage ignition. Black broken lines on contour images depict stoichiometry line.

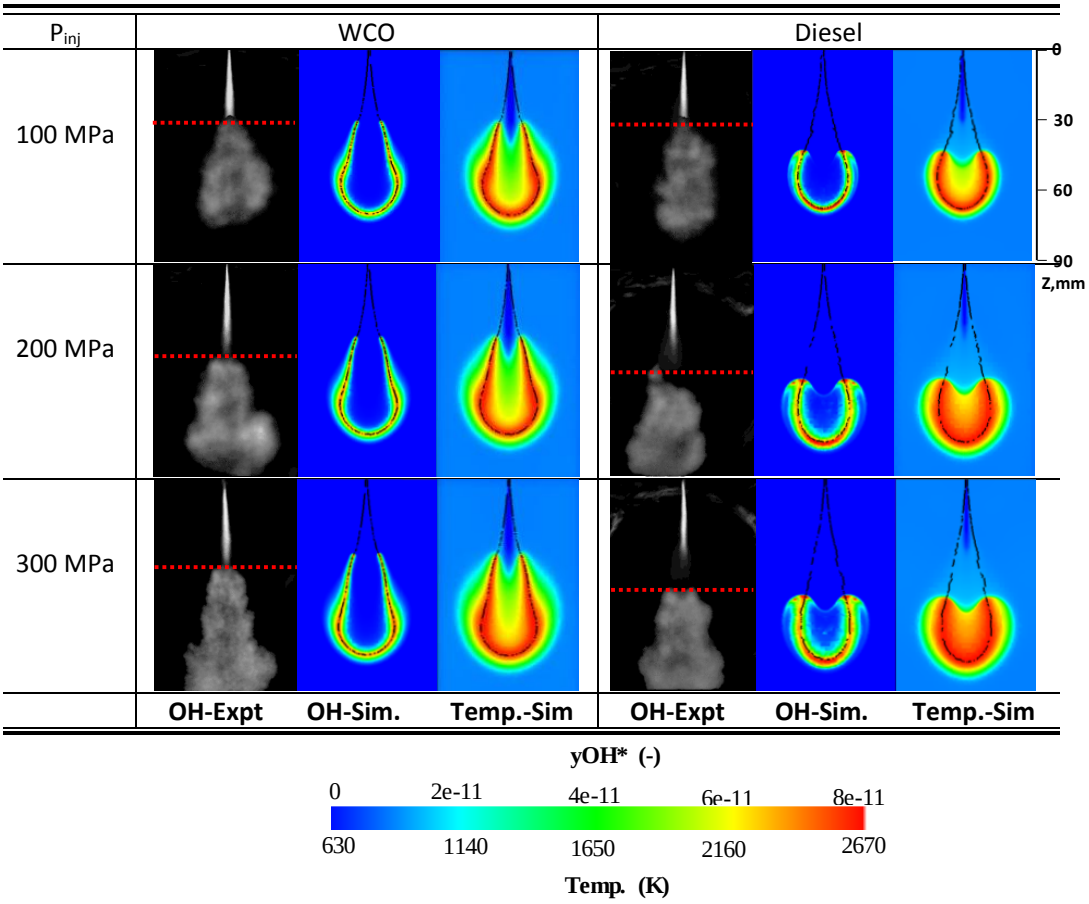

Figure 8 Variation of predicted lifted flames during injection event (1.4ms ASOI) with injection pressure validated with experiment. Experimental lifted flames are in grey (left) while simulated lifted flames are depicted by contour images (right). Black broken lines on contour images depict stoichiometry lines while the broken lines on experimental images show the location of the lifted flame.

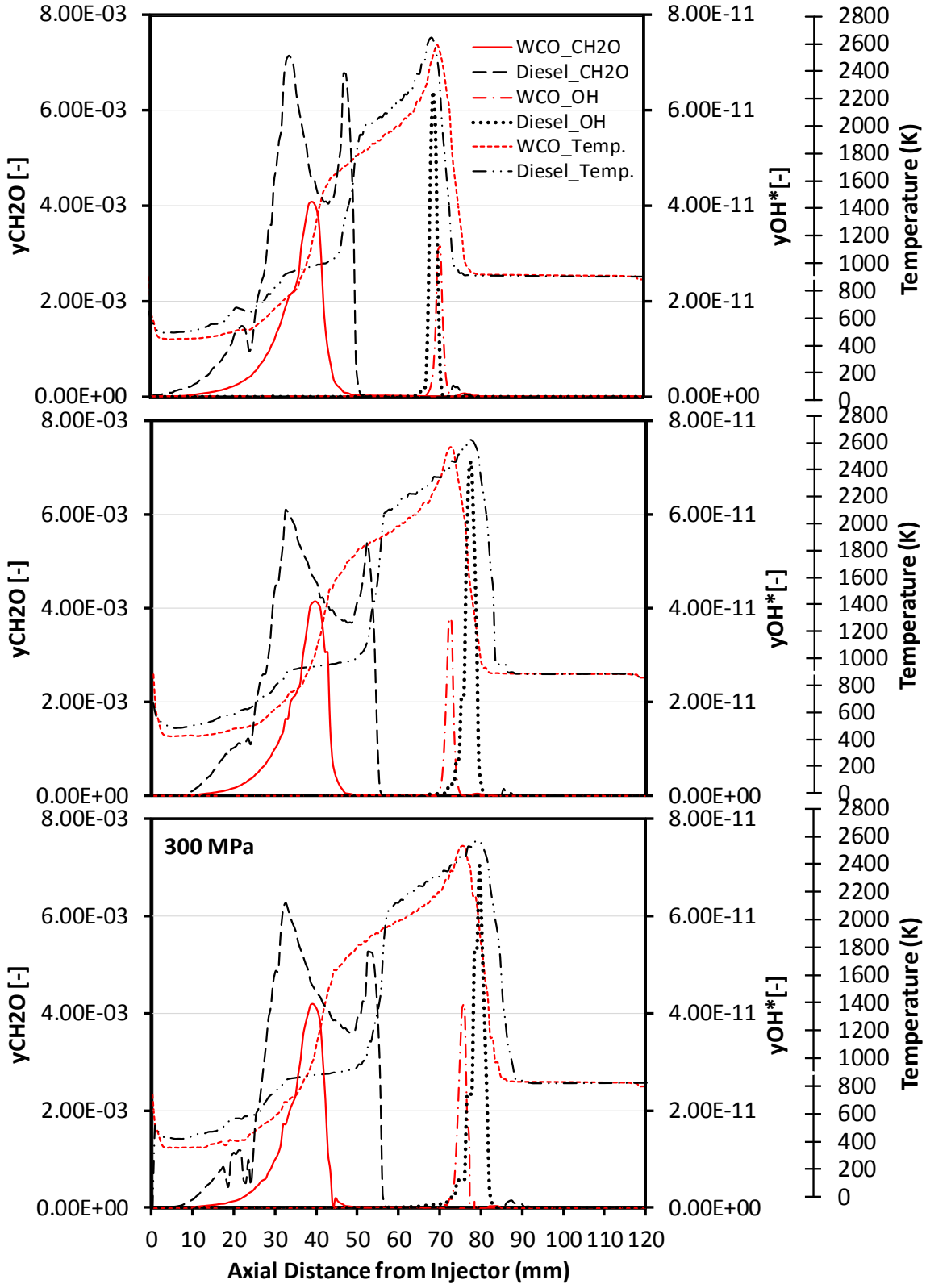

Figure 9 Axial variations of flame temperature, CH_2O and OH*species with injection pressure at 1.4ms ASOI.

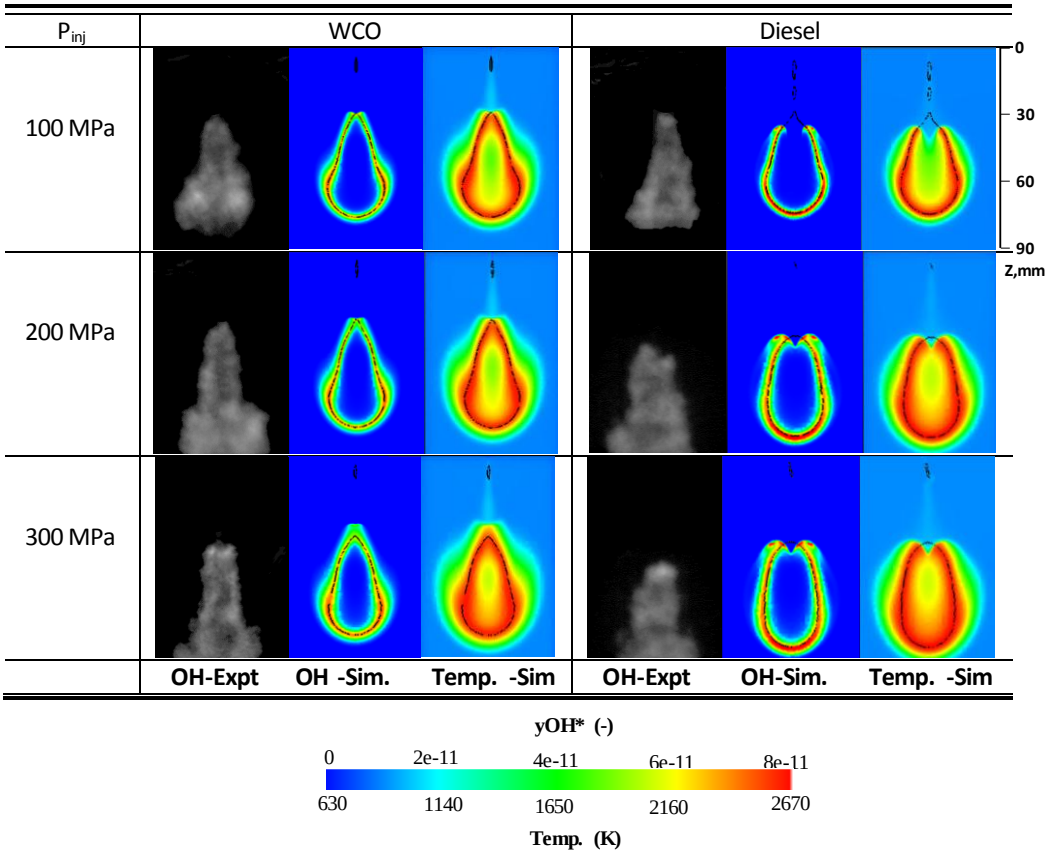

Figure 10 Variations of predicted lifted flames with injection pressure after end of injection (0.25 ms AEOI) validated with experiment. Experimental lifted flames are in grey (left) while simulated lifted flames are depicted by contour images (right). Black broken lines on contour images depict stoichiometry lines

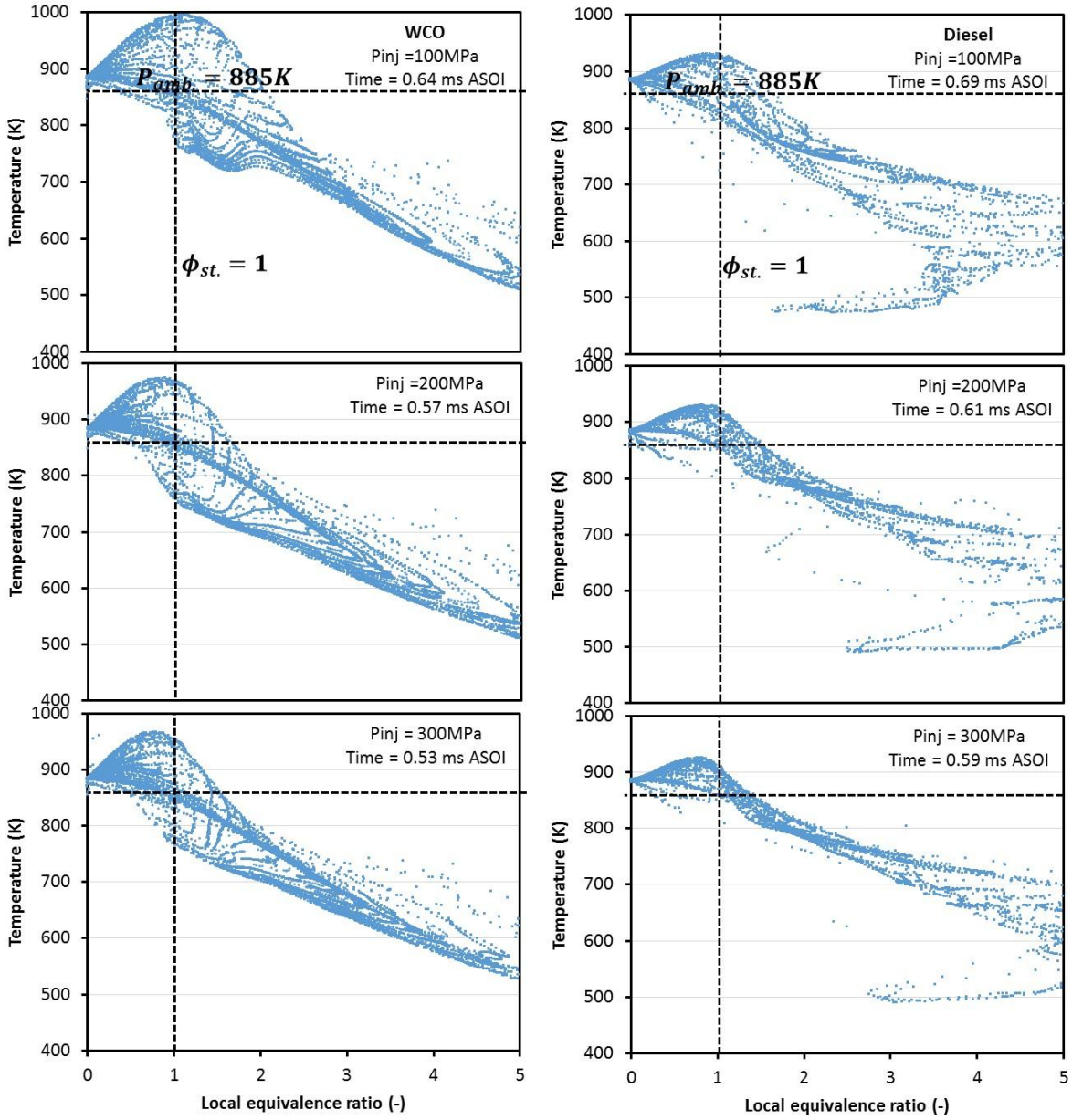

Figure 11 Variations of temperature with equivalence ratio at the first stage of ignition

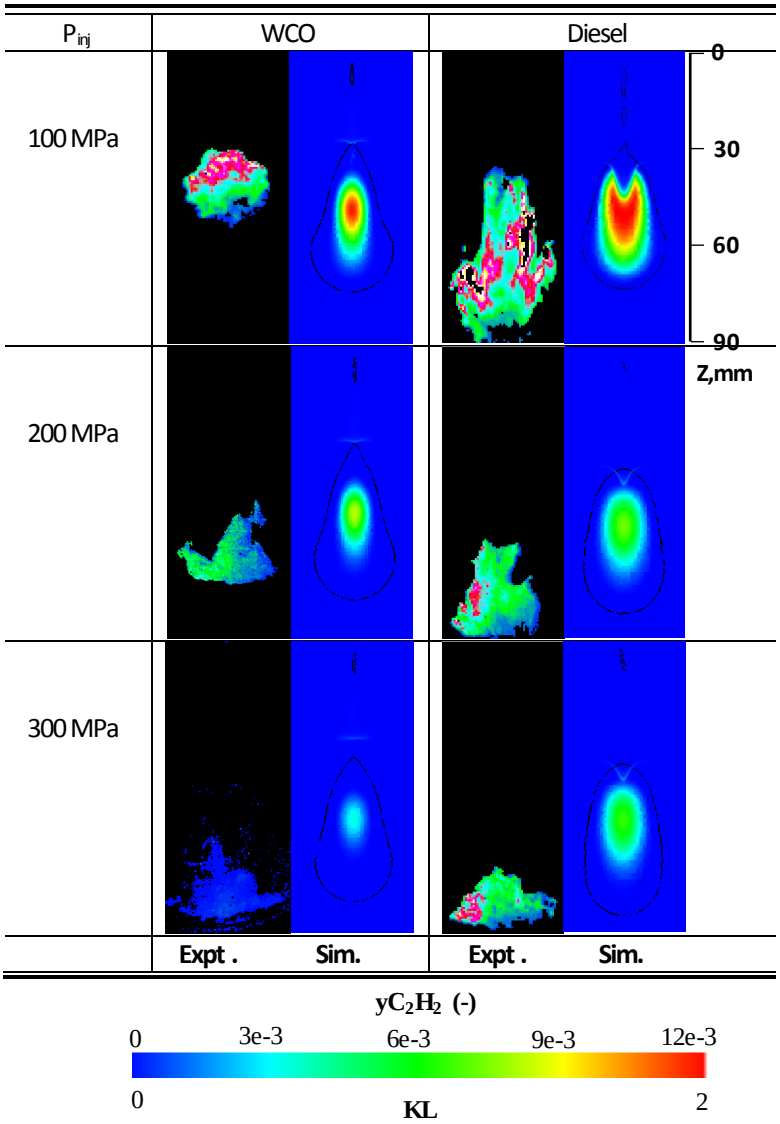

Figure 12 Variations of predicted soot formed with injection pressure after end of injection (0.25 ms AEOI) validated with experiment. Experimental lifted flames are in grey (left) while simulated lifted flames are depicted by contour images (right). Black broken lines on contour images depict stoichiometry lines

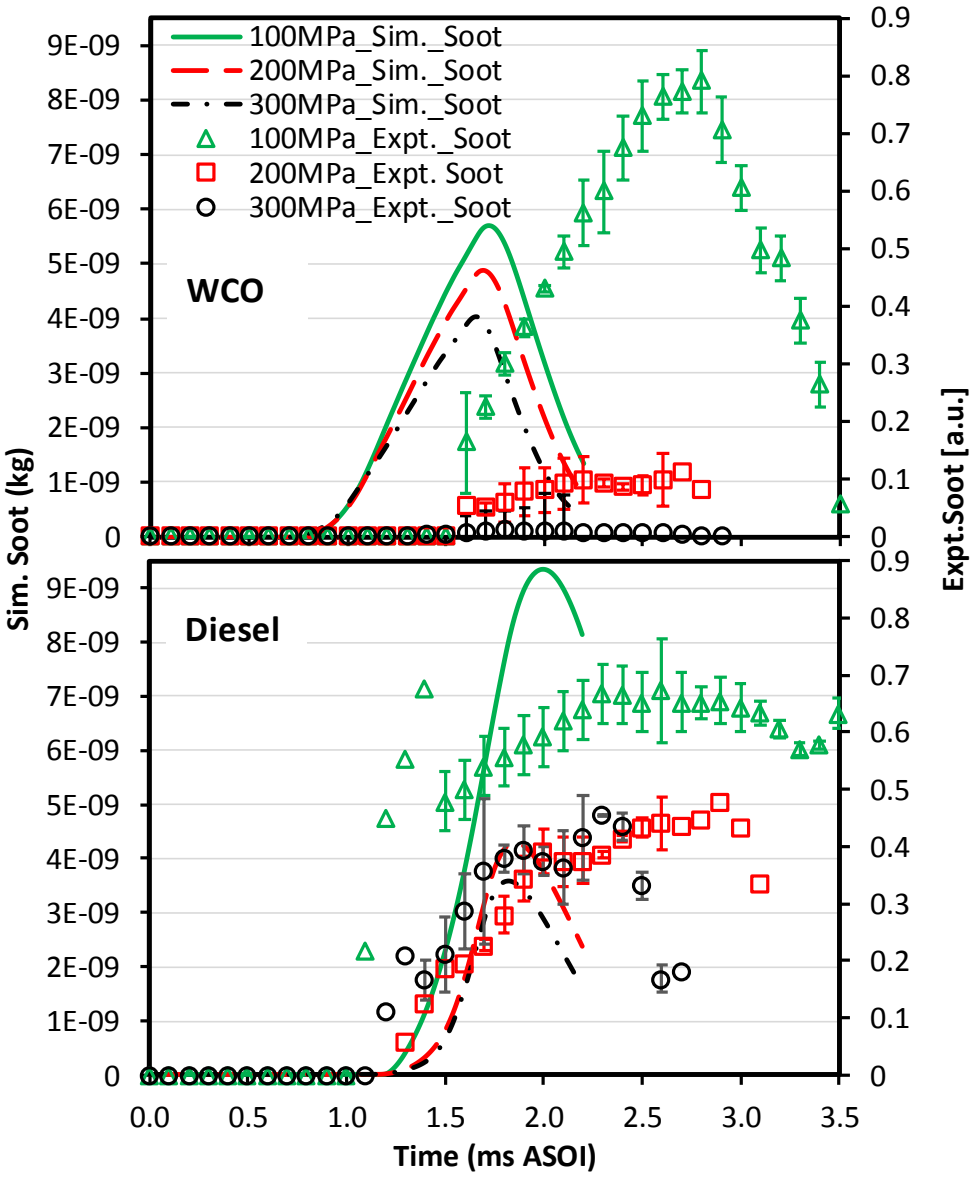

Figure 13 Temporal variations of predicted soot formed with injection pressure validated with experiment

Supplementary Material

Click here to download Supplementary Material: Supplementary data.docx

***Declaration of Interest Statement**

Declaration of interests

☒ The authors declare that they have no known competing financial interests or personal relationships that could have appeared to influence the work reported in this paper.

☐The authors declare the following financial interests/personal relationships which may be considered as potential competing interests:

***Author Contributions Section**

CRediT author statement

Olawole Abiola Kuti: Conceptualization, Methodology, Software, Validation , Data curation, Writing- Original draft preparation

S. Mani Sarathy: Software, Writing- Reviewing and Editing

K. Nishida: Supervision and Editing